1996

The flow diffusion nucleation chamber: A quantitative tool for nucleation research

Vivek Vohra

Richard H. Heist
Fairfield University, rheist@fairfield.edu

Published Citation

Vohra, V., & Heist, R. H. (1996). The flow diffusion nucleation chamber: A quantitative tool for nucleation research. The Journal of chemical physics, 104(1), 382-395. doi:10.1063/1.470837.

The flow diffusion nucleation chamber: A quantitative tool for nucleation research

Vivek Vohra and Richard H. Heist[a)]
Department of Chemical Engineering, University of Rochester, Rochester, New York 14627-0166

(Received 14 March 1995; accepted 29 September 1995)

We have developed a flow diffusion nucleation chamber designed to quantitatively investigate the nucleation of vapors. The design and operational characteristics of the nucleation chamber are presented and discussed. Critical supersaturation data obtained with this nucleation chamber are compared to literature data obtained using a thermal diffusion cloud chamber. The flow nucleation chamber results accurately reproduce the diffusion cloud chamber data. Results of preliminary measurements of nucleation at ambient pressure in the presence of different background gases are presented. These data suggest that the nature of the background gas may influence nucleation at ambient pressure. These data, while still of a preliminary nature, are consistent with data already published obtained at elevated pressures using a specially designed high pressure cloud chamber also in our laboratory. © *1996 American Institute of Physics.* [S0021-9606(96)03601-4]

I. INTRODUCTION

There are a variety of experimental devices used (or that have been used) for nucleation research.[1] Perhaps the two most commonly used for quantitative critical supersaturation and nucleation rate measurements are the thermal diffusion cloud chamber (TDCC) and the expansion cloud chamber (ECC). While these devices have been (and continue to be) useful in making quantitative nucleation measurements, they have limitations that impact upon their range of applicability and their overall usefulness. For instance, the TDCC can only be used to measure relatively small rates of nucleation (even if latent heat effects and vapor depletion are accounted for).[2,3(a),3(b)] Also, there are now serious questions of TDCC stability that could well limit the range of useful operation (at least at lower temperatures) to total pressures of approximately 1–2 bar and less.[4] Furthermore, although operation at higher temperatures and higher total pressures has been demonstrated using a specially designed high pressure thermal diffusion cloud chamber (HPCC) producing (possibly) quite remarkable results,[5–9] more study is required to determine the range of stable operation at these pressures and temperatures and, consequently, the validity of those results so obtained. In all these cases, however, the need to suppress convection in the diffusion cloud chamber demands that only light background gases be used or that, if somewhat heavier background gases are used, they be used only over limited ranges of pressure and temperature thus limiting the general applicability of the device. The expansion cloud chamber is capable of using a wide range of background gases,[10] however, it is also quite limited in the range of accessible pressures and temperatures.[11,12] In general, total pressures during nucleation are less than ambient and the accessible range of total pressure is small. Quite low nucleation temperatures are achievable, but it is often difficult to obtain data at nucleation temperatures much above ambient. Large nucleation rates are possible with expansion cloud chambers, but the range of the nucleation rate data does not overlap that achievable with the diffusion cloud chamber. Both the expansion and diffusion cloud chambers require significant amounts of thermodynamic and hydrodynamic property data (for pure components and their mixtures) as functions of temperature and (more recently) pressure. Often these data are not available and predictive methods must be used. Finally, it is difficult to collect and retrieve the nucleated particles using either of these two kinds of devices. The increasing interest in the chemical and physical properties of small particles (usually generated by nucleation processes) emphasize the importance of being able to retrieve and examine nucleated particles.

Flow nucleation devices offer a number of significant advantages over the diffusion cloud chamber and expansion cloud chamber systems just discussed. While they are, of course, not without problems, they can quite often be used effectively to produce results not easily achievable with the TDCC and ECC and also to provide important complementary results to those obtained with the TDCC and ECC devices. We shall address these issues in this paper.

Our eventual goals in this area of nucleation research are to have an instrument that will: (1) permit nucleation measurements (critical supersaturation and nucleation rate) to be made in the presence of a variety of background gases over wide ranges of temperature and pressure; (2) allow quantitative critical supersaturation measurements and nucleation rate measurements (over a range complementary to that obtainable with the TDCC and the ECC) in a flow-based system with convenient optical access to the nucleation region inside the chamber; and, (3) permit collection and retrieval of nucleated particles.

Our objectives in this particular investigation are: (1) to design, analyze, and test a version of this flow nucleation chamber that will allow critical supersaturation measurements using a variety of background gases at ambient pressure and a conveniently accessible range of temperatures; (2) to test the quantitative operation of the nucleation chamber by comparing nucleation measurements with data in the literature obtained using other nucleation devices; and, (3) to

a)Author to whom all correspondence should be addressed.

 0021-9606/96/104(1)/382/14/$6.00

make preliminary measurements of nucleation in the presence of a variety of different background gases and compare those results with data in the literature obtained using a specially designed high pressure cloud chamber.

In this paper we describe the design, construction, and operation of a flow diffusion nucleation chamber (FDNC) used to make nucleation measurements at approximately 1 bar total pressure and over the 305–330 K temperature range. These limited ranges of pressure and temperature are not fundamental limitations to FDNC operation. They are chosen for convenience in this investigation in order to allow detailed examination of the operational characteristics and behavior of this flow chamber design. The next step will be to modify the nucleation chamber to allow for operation over extended ranges of both pressure and temperature. In Sec. II the design and construction of the FDCC will be discussed, and the mathematical description of the operation of the FDCC will be presented. In Sec. III, experimental results from our investigations of the nucleation of 1-propanol in the presence of a variety of background gases are presented. In Sec. IV the results of these various measurements are discussed both in the context of the operation of the FDNC and in the context of conflicting experimental results from the literature describing nucleation in the presence of different background gases. Finally, our conclusions concerning the results of this investigation are presented in Sec. V.

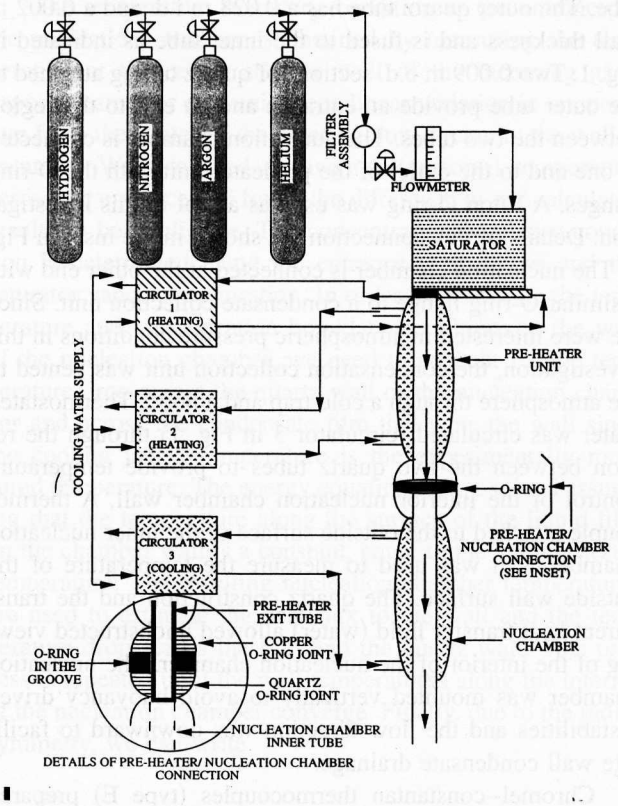

FIG. 1. Schematic diagram of the flow diffusion nucleation chamber used in this investigation. The inset provides details of the preheater/nucleation chamber connection (see the text for discussion).

II. FLOW DIFFUSION NUCLEATION CHAMBER

A. Design and operation

The flow diffusion cloud chamber developed and used in this investigation is shown schematically in Fig. 1.[13] Essentially, it is composed of a saturator unit, a vapor–gas preheater unit, and a nucleation chamber. The associated gas handling system, temperature control units, and measurement instrumentation make up the remainder of the experiment system.

The saturator unit is of rectangular geometry, 0.147 m long×0.083 m wide×0.076 m high and constructed from a standard 0.05-in.-thick brass sheet. The interior of the unit contains a series of 0.076 m high brass baffles each covered with a porous, cotton wicking fabric designed to provide a long path length (and, hence, a long residence time) for the gas flow and a large, moist surface area to ensure a saturated vapor–gas mixture entering the preheater unit. A thermocouple inserted in the saturator unit is used to measure the liquid temperature. The exterior is completely covered with insulating material to ensure isothermal operation. Temperature control is maintained by a circulating, thermostated heat transfer fluid (circulator 1 in Fig. 1) through a channeled, copper block bonded directly to the base of the saturator with thermal adhesive paste. The unit has been tested using gas chromatographic techniques to ensure that the vapor–gas flow exiting the saturator is saturated at the flow rates used in this investigation.

The function of the preheater unit is to control the temperature of the vapor–gas flow stream entering the nucleation chamber and to ensure that condensation does not occur prior to the flow stream entering the nucleation unit. The preheater unit is of cylindrical, double-walled geometry consisting of two concentric copper tubes. The outer tube has a standard 1.032 in. i.d. and the inner tube a standard 0.550 in. i.d.; each having a standard 0.062 in. wall thickness. The preheater is connected at one end to the saturator unit with a standard 0.5 in. threaded brass pipe coupling and at the other end to the nucleation chamber with a brass O-ring flange. It is 0.28 m in length. Thermostated, heat transfer fluid (circulator 2 in Fig. 1) circulating through the outer wall of the preheater is used to control the temperature of the unit. The entire unit is thermally insulated to maintain isothermal operation. Thermocouples located at the center and the wall of the preheater exit are used to measure the temperature of the vapor–gas mixture entering the nucleation chamber.

The function of the nucleation chamber is to generate vapor supersaturation which in turn promotes nucleation. A schematic diagram of the nucleation chamber is also shown in Fig. 1. The design used in this investigation was chosen to allow unobstructed viewing of the nucleation zone (thus achieving one of our overall goals) and to facilitate a quantitative description of the temperature and supersaturation conditions throughout the nucleation chamber. The nucleation chamber is of cylindrical, double-walled geometry and consists of a concentric set of quartz tubes. The inner tube is 0.108 m long with a 0.015 m i.d. and a 0.002-m-thick wall. Quartz O-ring flanges are attached to each end of the inner

tube. The outer quartz tube has a 0.028 m i.d. and a 0.002 m wall thickness and is fused to the inner tube as indicated in Fig. 1. Two 0.009 m o.d. sections of quartz tubing attached to the outer tube provide an entrance and an exit to the region between the two tubes. The nucleation chamber is connected at one end to the outlet of the preheater unit with the O-ring flanges. A Viton O-ring was used as a seal in this investigation. Details of this connection are shown in the inset in Fig. 1. The nucleation chamber is connected at the other end with a similar O-ring flange to a condensate collection unit. Since we were interested in atmospheric pressure conditions in this investigation, the condensation collection unit was vented to the atmosphere through a cold trap and a hood. Thermostated water was circulated (circulator 3 in Fig. 1) through the region between the two quartz tubes to provide temperature control of the interior nucleation chamber wall. A thermocouple attached to the outside surface of the inner nucleation chamber wall was used to measure the temperature of the outside wall surface. The quartz construction and the transparent heat transfer fluid (water) allowed unobstructed viewing of the interior of the nucleation chamber. The nucleation chamber was mounted vertically to avoid buoyancy driven instabilities and the flow direction was downward to facilitate wall condensate drainage.

Chromel–constantan thermocouples (type E) prepared from wire obtained from Omega Engineering were calibrated and used for all temperature measurements. A Leeds and Northrup, K-3, universal potentiometer and a Leeds and Northrup, model 9828, null detector were used to measure thermocouple voltages. Volumetric flow rates for the background gases were measured using flow meters obtained from Omega Engineering (model FL-3461). The flowmeters were calibrated with the gases used in this investigation prior to the experiments. HAAKE constant temperature circulator baths (baths 1, 2 and 3 in Fig. 1) were used to circulate thermostated heat transfer fluids for temperature control. Water was used as the heat transfer fluid for all the experiments in this investigation.

Conceptually, the flow chamber functions in the following manner: A stream of inert gas, e.g., argon, is first saturated with the vapor of the substance of interest, e.g., 1-propanol. This saturated flow stream then enters the preheater and is heated slightly above the saturator temperature. As this (slightly undersaturated) flow leaves the preheater and enters the nucleation chamber, the (relatively warm) vapor diffuses to the wet, cooler walls of the nucleation chamber where it condenses. Energy is transported to the walls thus cooling the flowing stream. Because of the relatively strong dependence of vapor pressure on temperature, the cooling of the vapor in the flow stream initially dominates vapor loss by diffusion to the walls and results in supersaturation of the vapor in a region downstream from the entrance to the nucleation chamber. The location of the supersaturated region also depends upon the flow stream velocity. As the vapor–gas mixture flows further down the tube, conditions are eventually reached where the temperature and vapor supersaturation become uniform across the nucleation chamber reflecting conditions existing at the temperature of the nucleation chamber wall.

B. Model equations

The differential equations describing the energy and mass transfer processes occurring in the nucleation chamber written for a cylindrical tube of circular cross section are

$$\frac{\partial}{\partial z}(\rho c_p v_z T)=\frac{1}{r}\frac{\partial}{\partial r}\left(kr\frac{\partial T}{\partial r}\right)+\frac{\partial}{\partial z}\left(k\frac{\partial T}{\partial z}\right) \tag{1}$$

and

$$\frac{\partial}{\partial z}(v_z C)=\frac{1}{r}\frac{\partial}{\partial r}\left(rD_{12}\frac{\partial C}{\partial r}\right)+\frac{\partial}{\partial z}\left(D_{12}\frac{\partial C}{\partial z}\right), \tag{2}$$

respectively. In Eq. (1) ρ and C_p are the mixture density and heat capacity, respectively. V_z is the axial component of the flow velocity, T is the mixture temperature, k is the mixture thermal conductivity, r is the chamber radius, and z is the axial dimension. In Eq. (2), C is the vapor concentration and D_{12} is the binary diffusion coefficient.

The term on the left-hand side of each of these equations accounts for convective transport in the axial direction. The first term on the right-hand side accounts for radial conductive transport and the second term on the right-hand side is a second-order term accounting for axial dispersion.

In order to solve Eqs. (1) and (2), we assume that a fully developed, parabolic velocity profile is established instantaneously at the entrance to the nucleation chamber. Since the gas–vapor mixture flows through the preheater (0.28 m) prior to entering the nucleation chamber, and since the transition length for our flow conditions is of the order of a few tenths of a centimeter, and since the region of interest in our investigations is several centimeters down the tube, the assumption of a fully developed, parabolic velocity profile at the entrance of the nucleation chamber appears reasonable. We note that we have also used the Langhaar approach,[14] which employs a linearizing approximation across the transition region. The difference in temperature profiles obtained using the fully developed velocity profile and the Langhaar profile was only 0.04 °C in the worst case. Differences in calculated supersaturation profiles were only in the third decimal place.

For this version of the flow chamber design and chamber analysis, Eqs. (1) and (2) were further simplified by ignoring the axial dispersion terms in favor of the radial conduction and forced axial convection contributions. Although much work has been reported in the literature dealing with the relative importance of axial dispersion and providing a sound basis for ignoring the dispersion contribution to the solution of Eqs. (1) and (2), we used a fluid dynamics computational program (FIDAP) to assess the importance of the axial dispersion term in our particular application. FIDAP (Fluid Dynamics Analysis Package) is a commercially available software package developed by Fluid Dynamics International. The FIDAP software uses a finite element-based method to numerically solve the general energy balance shown in Eq. (1). By solving Eq. (1) without the axial dispersion term (using

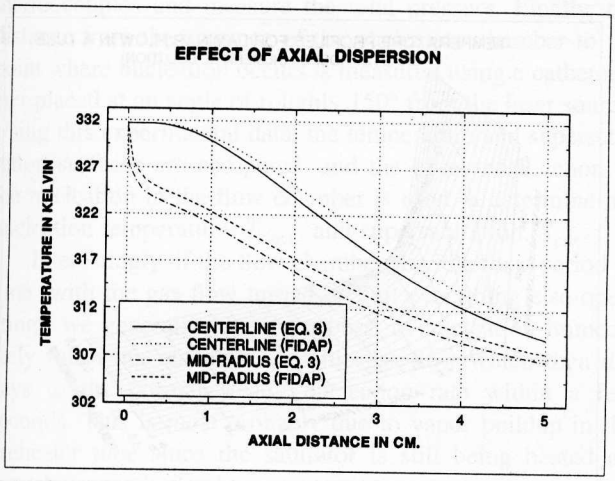

FIG. 2. Effect of axial dispersion in the flow diffusion nucleation chamber. Computed centerline and mid-radius axial temperature profiles obtained using FIDAP (see the text) and using Eq. (3) are shown.

our algorithm) and comparing that solution with the FIDAP generated solution (employing a parabolic velocity profile in each case), we were able to examine the relative importance of the axial dispersion term in our analysis. In Fig. 2, we compare the centerline and mid-radius temperature profiles obtained using both these approaches.

As can be seen in Fig. 2, the temperature profiles obtained using FIDAP when the axial dispersion term is included are slightly higher than the temperature profiles obtained ignoring the axial dispersion term (our numerical solution). This observation is consistent with similar observations reported in the literature.[15] For example, Kostrovskii *et al.*[16] have examined the solution of the energy balance including the axial dispersion term for a similar flow chamber geometry. They report results indicating that nucleation chamber temperatures calculated when including axial dispersion are within a degree of solutions obtained ignoring the axial dispersion term. Furthermore, they indicate that supersaturations calculated including the dispersion contributions in Eqs. (1) and (2) differ only by 1%–2% from those values obtained ignoring the dispersion terms. Thus, we have ignored the axial dispersion terms in the solution of Eqs. (1) and (2).

As a result of these assumptions, Eqs. (1) and (2) reduce to

$$v_{\max}\left[1-\left(\frac{r}{R_t}\right)^2\right]\frac{\partial}{\partial z}T=\alpha\,\frac{1}{r}\,\frac{\partial}{\partial r}\left(r\,\frac{\partial T}{\partial r}\right) \tag{3}$$

and

$$v_{\max}\left[1-\left(\frac{r}{R_t}\right)^2\right]\frac{\partial}{\partial z}C=D_{12}\,\frac{1}{r}\,\frac{\partial}{\partial r}\left(r\,\frac{\partial T}{\partial r}\right), \tag{4}$$

respectively. The term, α, in Eq. (3) denotes the thermal diffusivity and is defined as

$$\alpha=\frac{k}{(\rho c_P)}. \tag{5}$$

The temperature boundary condition at the entrance to the nucleation chamber is obtained by measuring the temperature at the center and the wall of the incoming gas–vapor stream. For convenience, a linear variation in temperature from the center of the entering flow stream to the wall is assumed. We also used an average (uniform) temperature across the entrance and found the difference in our calculated results to be negligible. The concentration boundary condition is determined using the entrance temperature and the saturator vapor concentration. In order to determine the temperature and concentration boundary conditions at the wall of the nucleation chamber, we need to account for the temperature drop across the quartz wall of the nucleation chamber and across the condensate film that wets the wall since the cooling jacket temperature is the experimentally measured temperature. The energy equation is first solved assuming that the temperature along the surface of the liquid film on the chamber wall is a constant, equal to the cooling water temperature. The resulting nucleation chamber temperatures are used to estimate the heat flux to the wall and the temperature drop across the film and the quartz wall. This process is repeated until the wall temperatures along the interior of the nucleation chamber converge. Finally, due to the radial symmetry, we can write

$$\frac{\partial T}{\partial r}=0 \quad \text{at } r=0 \text{ for all } z, \tag{6a}$$

and

$$\frac{\partial C}{\partial r}=0 \quad \text{at } r=0 \text{ for all } z. \tag{6b}$$

In solving Eqs. (3) and (4), we include, where appropriate, the temperature and composition dependence of the heat capacity, thermal conductivity, gas phase density, and binary diffusion coefficient in the analysis. The mixture heat capacity was computed as a mole fraction weighted average of the heat capacities of the vapor and carrier gas heat capacities. The gas–vapor mixture density was determined assuming an ideal mixture. The mixture thermal conductivity was computed utilizing Wilke's kinetic theory relationship[17] and utilizing the Lindsey–Bromley prescription.[17] The thermodynamic and hydrodynamic property data used in our investigations are listed in Table V.

To assess the reliability of our solution method and the assumptions underlying Eqs. (3) and (4), we analyzed a well-known fluid flow problem for which analytical solutions exist in the literature. If we assume that our nucleation chamber wall temperature is constant and that the temperature of the gas stream entering the nucleation chamber is constant across the entrance, the problem of describing the temperature distribution in our nucleation chamber resembles that of the classic Graetz–Nusselt problem that has been studied extensively and for which there exist both analytical and numerical solutions. Due to computational limitations, the original Graetz solution to this problem consisted of only the first two terms of an infinite series.[18] This solution was later extended

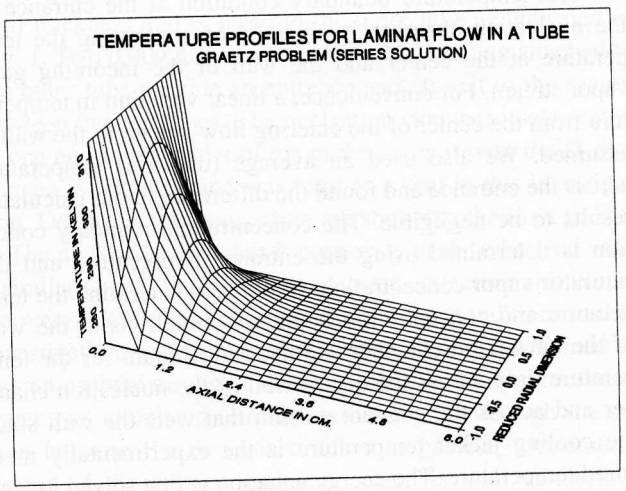

FIG. 3. Temperature profiles obtained for laminar flow through a tube using the series solution of the Graetz problem (see the text for discussion).

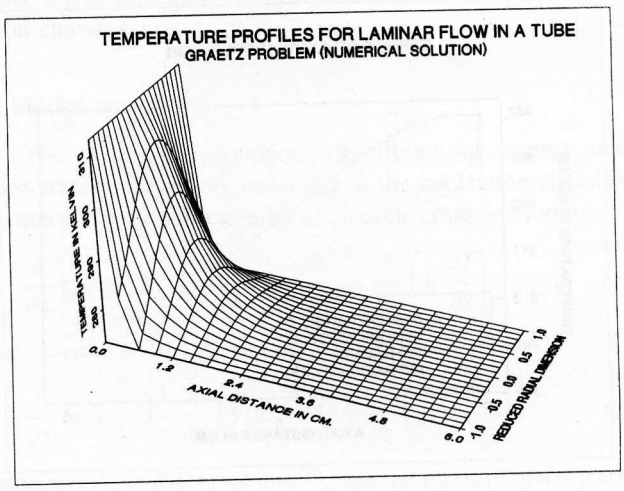

FIG. 4. Temperature profiles obtained for laminar flow through a tube using the numerical solution of the Graetz problem developed for this investigation (see the text for discussion).

by Nusselt to include 3 terms[19] and, subsequently, by other workers to include 5, 10,[20] and, eventually, 121 terms.[21]

To examine the solution to Eq. (3) in the context of the Graetz problem, we adopted the implicit finite difference method proposed by Crank and Nicholson[22] employing a variable grid in the axial direction. The method has proven to be convenient, stable, and quickly convergent.

We note that it has been reported that numerical solutions to the Graetz problem in the 0.000 01 m entrance region produce estimates of Nusselt numbers that are in error and that even the 121-term solution does not converge in this region.[21,23–26] However, our region of interest in the nucleation chamber is several centimeters down the chamber where, our preliminary calculations have shown, the maximum in the supersaturation profile will occur. Hence, the entrance distance of 0.000 01 m over which the Graetz solution exhibits poor agreement with numerical solutions can safely be ignored. If we compare temperature profiles obtained using our numerical method with those obtained using the 121-term series solution to the Graetz problem at a distance far from the entrance, we find excellent agreement as demonstrated by the plots shown in Figs. 3 and 4 for a typical set of chamber wall and flow stream temperature conditions. In the worst case, agreement is within 0.1% at distances of only 0.004 m into the nucleation chamber. Agreement improves rapidly further into the chamber. We have noticed that Nusselt numbers obtained from the analytic solution are somewhat lower than those obtained from the numerical solution near the entrance, but the agreement improves further into the chamber. This observation is consistent with trends reported in literature. Kays[23] points out that reliable experimental laminar flow temperature data for gases flowing in circular tubes is difficult to obtain. This observation explains, in part, why so few data are available for direct comparison with Graetz-type solutions.

Based on our analysis, comparisons with data for similar flow chambers described in the literature, and our comparisons with literature data for the Graetz problem, we conclude that our finite difference algorithm is suitable for the solution of Eqs. (3) and (4) to describe the temperature and concentration profiles in the nucleation chamber.

III. EXPERIMENT PROCEDURE

We chose 1-propanol as the working fluid for this investigation because there exists reliable critical supersaturation data over a wide range of temperatures and pressures.[2,5] This information will allow comparison of data obtained from measurements in this investigation and enable an evaluation of the operation of this flow chamber. The 1-propanol used in this investigation was Baker analyzed reagent grade. It was used without further purification. Hydrogen, helium, argon, and nitrogen were used as inert, background gases in this investigation. All gases were obtained from Air Products. The hydrogen was ultra pure carrier grade (99.999%); the helium was chromatographic grade (99.9999%); the argon was ultra pure carrier grade (>99.999%); and the nitrogen was ultra pure carrier grade (99.999%).

A. A typical experiment

To begin a typical experiment, the preheater unit is first brought to the desired temperature with thermostated fluid from circulator 2 to vaporize any propanol which might have collected in the tube between the saturator and the nucleation chamber. Next, the flow from circulator 1 to the saturator unit is started to bring the saturator to the desired temperature. Finally, we start the flow from circulator 3 to cool the walls of the nucleation chamber. The temperatures are adjusted so that the gas–vapor stream temperature at the entrance to the nucleation chamber is slightly higher than the temperature of the saturator. When these temperatures stabilize, the cooling water jacket temperature is adjusted until we observe droplet formation in the nucleation chamber at the (estimated) rate of 1–5 drops/cm^3/s. The nucleated droplets are observed by light scattered from an 8 mW He–Ne laser beam. At this point, we record the signals from the four

thermocouples and measure the total pressure. Finally, the distance from the entrance of the nucleation chamber to the point where nucleation occurs is measured using a cathetometer placed at an angle of roughly 150° from the laser source. Using this experimental data, the temperature and supersaturation surfaces are computed, and the observed location of the nucleation in the flow chamber is used to determine the nucleation temperature, T_{nucl}, and supersaturation, S_{crit}.

Interestingly, if the flow chamber sits idle for a period of time (with the gas flow turned off but everything else operating), we generally observe a burst of nucleation immediately following resumption of the gas flow which then decays to the normal steady nucleation rate within a few seconds. This is most probably due to vapor buildup in the preheater tube since the saturator is still being heated although no gas is flowing.

In our experiments, we observe that a steady rate of nucleation, localized in a specific axial region of the flow chamber (usually the center), is generally accompanied by a much smaller, irregular rate of formation of drops, which we refer to as background nucleation, located throughout the flow chamber. The steady nucleation localized in the center portion of the nucleation chamber is homogeneous nucleation and the background is most probably heterogeneous nucleation arising from the presence of condensation centers in the gas stream. If, for example, at a gas flow velocity of 0.02 m/s, we observe a steady rate of homogeneous nucleation occurring at a particular location in the nucleation chamber, then our model calculations predict that if the gas flow rate is increased to, say, 0.06 m/s, homogeneous nucleation will cease at that particular location and move further down the nucleation chamber to a new location. In fact, when we actually carried out this experiment, we observed that the location of the steady, localized nucleation was, indeed, a function of the gas flow velocity whereas the background nucleation was not. Furthermore, the homogeneous nucleation begins at a particular distance from the entrance to the nucleation chamber (as predicted by the model equations) whereas the background nucleation becomes visible nearly as soon as the warm gas–vapor mixture stream enters the nucleation chamber. The degree of background nucleation seemed to vary with different background gases, but did not appear to follow any particular pattern. The background nucleation was tested for ions by applying a 300 V dc field across the chamber. We observed no effect; thus we conclude that the droplets are not charged. Interestingly, inserting a 0.015 μ micron filter in the background gas flow before the saturation unit had no significant effect on the background nucleation. We have observed, however, that if the gas supply tank is not moved or agitated for a few days, then we detect less background nucleation; but if the tank is moved or agitated then we suddenly observe a significant increase in background nucleation.

IV. EXPERIMENT RESULTS

Initially, a series of experiments utilizing 1-propanol and helium were carried out to test the experiment setup, the flow chamber design, the temperature and supersaturation profile calculations, and to investigate the operational characteristics of the flow chamber. Following these experiments, a series of critical supersaturation versus temperature measurements were carried out using the 1-propanol/helium system in order to compare results obtained using the flow diffusion chamber with similar data obtained using a thermal diffusion cloud chamber.

The experimental data obtained from these measurements are listed in Table I. Here, the first column lists the run number, RN No., of the particular experiment; columns 2–5 list the temperature of the saturator, T_S, the temperature of the gas–vapor stream at the wall of the preheater unit as it enters the nucleation chamber, T_W, the centerline temperature of the gas–vapor stream entering the nucleation chamber, T_C, and the temperature of the nucleation chamber water jacket, T_J, respectively; column 6 lists the gas–vapor volumetric flow rate, F_R; column 7 lists the measured distance (from the entrance of the nucleation chamber) to the point where nucleation was observed in the nucleation chamber, D_N; column 8 lists the temperature in the chamber where nucleation was observed, T_{nucl}; and column 9 lists the supersaturation in the chamber where nucleation was observed, S_{crit}. The measured temperatures and flow velocities listed in Table I are used in the solution of Eqs. (3) and (4) to obtain the temperature and supersaturation profiles throughout the nucleation chamber in each experiment. As mentioned earlier, the measured distance, D_N, and the temperature and supersaturation surfaces were used to determine the supersaturation, S_{crit}, and the temperature, T_{nucl}, where nucleation was observed to occur.

The critical supersaturation and nucleation temperature data listed in Table I are plotted in Fig. 5. Also shown in Fig. 5, as dashed line curves, are critical supersaturation data from the literature for the 1-propanol/helium system obtained using a thermal diffusion cloud chamber.[2] The numbers assigned to these dashed lines refer to the run numbers specified in the original paper. An envelope drawn through these dashed line curves (not shown for the sake of clarity) would represent the measured variation of the critical supersaturation with temperature and would pass through the collection of points representing the data obtained in this investigation. For purposes of comparison, predictions of the Becker–Doering–Zeldovitch theory of homogeneous nucleation and a "scaled" version of that BDZ theory obtained from Ref. 2 for 1-propanol are also included in Fig. 5. We shall discuss this data further in Sec. V.

As mentioned earlier, there is much concern regarding (possible) effects of different background gases on the homogeneous nucleation of vapors. It was also explained that an eventual goal of this research was to be able to use different background gases in our nucleation experiments, and that an objective of this investigation was to make preliminary nucleation measurements using a variety of background gases. Toward these ends, we have carried out a series of critical supersaturation measurements with this flow diffusion chamber using 1-propanol and hydrogen, nitrogen, and argon as background gases (in addition to the helium experi-

TABLE I. Experimental FDCC data for the 1-propanol/helium system.

RN No.	Temperatures (K) T_{-S}	T_{-W}	T_{-C}	T_{-J}	F_{-R} (10^{-6} m^3/min)	D_{-N} (10^{-2} m)	$T_{-\text{nucl}}$ (K)	$S_{-\text{crit}}$
1	322.5	323.4	330.0	295.2	619.7	3.25	300.6	2.480
2	324.5	326.0	332.9	296.4	619.7	3.54	301.1	2.480
3	326.2	327.7	334.9	297.4	616.2	3.54	302.6	2.450
4	328.2	329.6	336.7	298.6	616.2	4.05	302.7	2.470
5	318.8	319.6	325.8	292.6	619.7	3.46	296.2	2.590
6	319.8	320.5	326.7	293.1	616.2	3.29	297.5	2.580
7	319.8	321.2	327.6	293.2	616.2	3.56	296.8	2.580
8	320.7	321.4	327.7	293.8	616.2	3.36	298.1	2.570
9	321.7	322.5	328.8	294.6	616.2	3.40	299.0	2.530
10	322.6	323.2	329.7	295.0	612.7	3.66	298.8	2.570
11	323.7	324.3	330.8	295.8	612.7	3.51	300.3	2.530
12	324.7	325.6	332.3	296.7	612.7	3.65	300.9	2.490
13	325.5	326.6	333.3	297.2	612.7	4.00	300.6	2.490
14	326.4	327.4	334.2	297.6	612.7	3.77	302.0	2.490
15	317.9	319.0	325.1	291.9	616.2	3.40	295.6	2.600
16	318.9	319.8	325.9	292.4	612.7	3.15	297.0	2.590
17	329.1	335.4	336.3	301.3	619.7	4.44	303.4	2.370
18	326.7	332.7	334.7	298.1	619.7	3.63	304.2	2.360
19	329.0	334.9	336.3	299.6	619.7	4.03	304.5	2.390
20	330.7	336.6	337.8	300.1	619.7	4.28	304.6	2.400
21	332.7	338.4	339.5	301.0	616.2	4.72	304.9	2.390
22	334.4	340.1	341.3	301.6	616.2	5.05	305.1	2.290
23	334.3	339.9	341.3	302.3	612.7	5.28	306.1	2.310
24	336.4	340.8	343.0	303.1	612.7	5.37	307.0	2.350
25	340.1	346.3	347.9	304.5	676.1	6.36	307.9	2.250
26	341.7	347.8	350.0	305.1	676.1	6.87	308.1	2.200
27	343.5	348.9	352.2	305.8	672.5	7.55	308.0	2.130

ments just described). The experimental data obtained from these measurements are listed in Tables II, III, and IV, respectively. As before, the first column in each table lists the run number RN No. of the particular experiment; columns 2–5 list the temperature of the saturator, T_S, the temperature of the gas–vapor stream at the wall of the preheater unit as it enters the nucleation chamber, T_W, the centerline temperature of the gas–vapor stream entering the nucleation chamber, T_C, and the temperature of the nucleation chamber water jacket, T_J, respectively; column 6 lists the gas volumetric flow rate, F_R; column 7 lists the measured distance (from the entrance of the nucleation chamber) to the point where nucleation is observed to begin in the nucleation chamber, D_N; column 8 lists the temperature in the chamber where nucleation was observed to occur, T_{nucl}; and column 9 lists the supersaturation in the chamber where nucleation was observed to occur, S_{crit}.

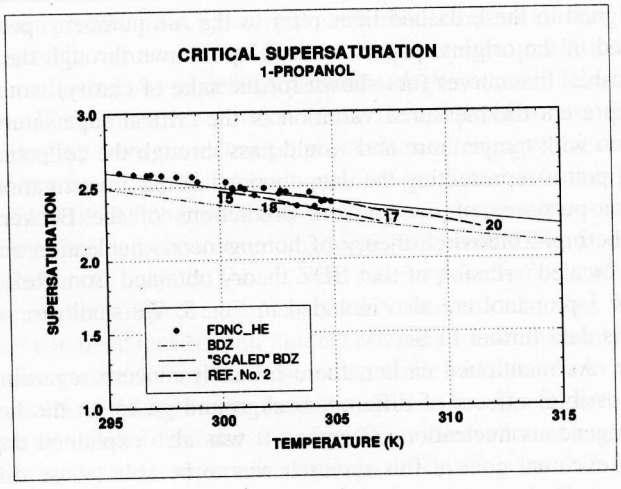

FIG. 5. Variation of the critical supersaturation of 1-propanol with temperature, using helium as the carrier gas in the FDNC (solid circles) compared with data obtained from thermal diffusion cloud chamber measurements (numbered dashed lines) described in Ref. 2. Predictions of the BDZ nucleation theory (dash dot dot dot line) and a "scaled" version of the BDZ theory (solid line) described in Ref. 2 are included for comparison only (see the text for discussion).

The critical supersaturation and nucleation temperature data listed in Tables II–IV are plotted in Fig. 6. Also shown in Fig. 6 are critical supersaturation data from the 1-propanol/helium experiments listed in Table I and described above. These data are included to facilitate comparison with the critical supersaturation data in Tables II–IV. For purposes of comparison, predictions of the Becker–Doering–Zeldovitch theory of homogeneous nucleation and a "scaled" version of that BDZ theory obtained from Ref. 2 for 1-propanol are also included in Fig. 6. We shall discuss this data further in Sec. V.

In order to describe conditions existing in the nucleation chamber during our experiments in more detail, representative three-dimensional, perspective plots of temperature, supersaturation, nucleation rate, and droplet density in the

TABLE II. Experimental FDCC data for the 1-propanol/argon system.

RN No.	Temperatures (K) T_{-S}	T_{-W}	T_{-C}	T_{-J}	F_{-R} (10^{-6} c/m^3/min)	D_{-N} (10^{-2} m)	$T_{-\mathrm{nucl}}$ (K)	$S_{-\mathrm{crit}}$
28	342.1	343.4	347.1	298.1	305.5	8.28	313.9	2.007
29	344.1	345.2	349.1	298.5	274.2	7.58	314.8	2.012
30	345.9	346.9	351.3	299.2	274.2	7.80	315.8	1.987
31	346.1	347.0	351.6	299.2	274.2	8.10	317.9	1.909
32	347.8	349.3	354.1	300.1	309.2	8.67	317.9	1.902
33	349.4	351.0	356.4	300.0	329.6	9.00	319.2	1.875
34	336.6	337.6	340.9	295.9	301.8	7.78	310.2	2.074
35	339.0	340.0	343.9	296.8	301.8	7.78	312.9	2.029
36	340.0	340.5	345.2	296.8	340.7	8.60	313.4	2.014
37	341.1	342.1	347.1	297.2	342.6	8.84	314.2	1.981
38	342.1	342.6	347.9	298.1	309.2	8.34	314.0	1.998
39	343.0	345.1	349.3	297.7	338.9	8.70	315.9	1.928
40	337.2	338.3	341.9	295.7	322.2	7.94	311.5	2.039
41	338.3	339.2	343.0	296.2	324.0	8.64	310.6	2.091
42	339.1	340.1	343.9	296.7	324.0	8.18	312.7	2.019
43	340.1	340.8	344.9	296.6	331.5	8.56	312.8	2.054
44	341.1	342.2	346.5	297.0	331.5	8.71	313.4	2.029

nucleation chamber obtained for experiment RN 3 in which helium was used as the background gas and experiment RN 43 in which argon was used as the background gas are shown in Figs. 7–10 and 11–14, respectively.

V. DISCUSSION

An examination of the representative three-dimensional, perspective plots reveals a number of salient points concerning the operation of the flow diffusion chamber. From Figs. 7 and 11, it is seen that the temperature is maximum in the upper region of the nucleation chamber where the gas–vapor flow from the preheater enters. It is also seen that the temperature decreases from the center to the wall across the entrance to the nucleation chamber. The extent of this temperature drop depends upon the thermal properties of the gas–vapor mixture and the difference between the preheater

TABLE III. Experimental FDCC data for the 1-propanol/nitrogen system.

RN No.	Temperatures (K) T_{-S}	T_{-W}	T_{-C}	T_{-J}	F_{-R} (10^{-6} m^3/min)	D_{-N} (10^{-2} m)	$T_{-\mathrm{nucl}}$ (K)	$S_{-\mathrm{crit}}$
45	336.5	337.3	344.0	294.0	398.3	10.47	307.6	2.160
46	338.5	340.8	346.5	295.9	380.2	11.22	307.2	2.130
47	339.5	341.6	345.9	296.3	312.7	10.83	304.4	2.220
48	340.4	342.7	345.9	296.4	286.2	10.65	303.5	2.230
49	341.3	343.3	348.6	296.7	366.6	11.95	306.7	2.200
50	342.3	344.2	349.3	297.2	366.6	12.62	306.3	2.210
51	343.6	345.4	345.0	297.1	277.5	11.96	302.3	2.260
52	344.4	346.1	345.9	297.2	273.1	11.90	302.3	2.280
53	342.0	344.3	348.2	297.5	366.6	11.85	307.8	2.160
54	337.5	340.2	345.8	296.1	362.1	11.00	306.3	2.100
55	338.5	341.5	346.9	296.6	364.4	11.45	306.3	2.100
56	339.5	342.4	347.8	297.1	364.4	11.77	306.6	2.090
57	340.4	343.3	348.3	297.5	366.6	12.12	306.8	2.100
58	341.3	344.3	349.7	297.1	402.8	12.10	309.0	2.090
59	342.2	344.9	349.9	297.7	371.1	11.90	308.3	2.110
60	343.1	346.1	350.8	297.6	371.1	12.41	307.8	2.160
61	343.6	346.5	351.1	298.1	357.6	13.30	306.0	2.150
62	344.6	347.9	346.9	297.6	326.1	12.82	304.6	2.280
63	337.6	340.0	344.9	296.3	353.1	11.06	305.7	2.120
64	338.5	340.8	345.8	296.6	355.3	11.28	306.1	2.130
65	340.2	343.0	347.5	296.8	350.8	11.85	305.7	2.160
66	341.2	343.9	348.1	297.2	350.8	12.45	305.3	2.170
67	342.1	344.7	348.9	297.3	353.1	12.03	306.6	2.180
68	343.0	345.8	349.8	297.4	353.1	12.11	306.8	2.200
69	344.0	346.5	350.7	297.7	359.9	12.54	307.2	2.200

TABLE IV. Experimental FDCC data for the 1-propanol/hydrogen system.

RN No.	Temperatures (K) T_{-S}	T_{-W}	T_{-C}	T_{-J}	F_{-R} (10^{-6} m^3/min)	D_{-N} (10^{-2} m)	$T_{-\text{nucl}}$ (K)	$S_{-\text{crit}}$
70	335.6	341.1	344.6	297.2	934.8	8.32	300.5	2.510
71	337.2	340.9	346.4	298.1	921.0	8.75	300.9	2.440
72	339.3	340.1	351.7	298.7	969.9	9.17	302.1	2.450
73	340.5	347.0	351.2	298.7	962.9	9.89	301.4	2.410
74	341.4	348.1	352.2	299.3	1086.4	10.05	303.6	2.440
75	342.8	349.2	353.7	299.3	1005.6	10.30	302.5	2.420
76	344.5	351.1	355.8	299.9	1005.6	10.67	303.0	2.380
77	348.5	355.1	360.2	300.7	1012.8	11.82	303.6	2.320
78	335.3	336.2	346.9	298.6	955.8	8.15	302.1	2.380
79	337.5	343.7	347.3	298.6	1012.8	8.46	303.2	2.440
80	339.7	345.6	349.5	299.2	1012.8	9.30	303.0	2.420
81	339.2	346.2	350.2	299.5	1101.4	10.22	303.1	2.350
82	338.9	345.0	349.1	299.7	1257.2	10.66	304.5	2.360
83	342.0	346.4	350.4	300.1	1109.0	10.44	304.1	2.410
84	343.0	348.3	352.6	300.6	1109.0	10.89	304.3	2.350
85	345.4	350.1	354.7	301.1	1101.4	11.23	305.0	2.330
86	340.6	343.6	347.9	299.5	955.8	9.59	302.3	2.400

and the cooling jacket temperatures. A simple linear approximation was used to link the measured centerline and wall temperatures for use in our analysis. Although the temperature of the water jacket surrounding the nucleation chamber (see Fig. 1, above) is constant, there is a small variation in the temperature of the condensation film along the length of the nucleation chamber wall because of the varying energy flux to the wall and the resulting temperature drop across the condensate film and the chamber wall. The radial temperature profile at different points along the axial dimension in the nucleation chamber decreases gradually, becoming flatter toward the chamber exit. By comparing the axial scales in Figs. 7 and 11, we note that the temperature profile drops off more rapidly when helium is used as the background gas than when argon is used. This is consistent with helium having the higher thermal conductivity.

In Figs. 8 and 12, we see that the supersaturation rises from slightly less than one at the entrance to the nucleation chamber to a maximum value and then decreases further down the chamber. In RN 3, when helium was used as the background gas, the maximum in the supersaturation occurred at approximately 0.048 m from the nucleation chamber entrance. In RN 43, when argon was used as the background gas, the maximum in the supersaturation was found to be approximately 0.124 m from the entrance. In each case the supersaturation profiles flatten out toward the end of the nucleation chamber as the vapor concentration approaches equilibrium at the wall temperature. The observation that the maximum in the supersaturation profile obtained using argon occurred further down the nucleation chamber than when helium was used is due, in large part, to the difference in the temperature profiles and the difference in the binary diffusion coefficients of 1-propanol in argon and helium. The excursions in supersaturation evident in Figs. 8 and 12 near the entrance to the nucleation chamber and immediately below the end of the preheater walls arise because there is a discontinuous change (reduction) in the boundary temperature as the gas–vapor mixture passes from the warmer preheater section into the nucleation chamber. The wall temperature in the nucleation chamber is significantly cooler than the wall of the preheater and this discontinuous change to a cooler wall temperature is "felt" first by the gas–vapor flow near the wall thus producing a (localized) excursion to a larger supersaturation. As the gas–vapor flow proceeds further down the nucleation chamber, more and more of the flow feels the cooler wall temperature and the excursion is reduced as the supersaturation profile assumes the smoother shape evident in each of the figures. The difference in the magnitude of the excursions shown in Figs. 8 and 12 is primarily due to differences in the temperature drop from the preheater exit to the nucleation chamber wall and the properties of the two background gases. Similar results are obtained for the hydrogen and nitrogen systems.

In Figs. 9 and 13, the predicted nucleation rate [computed using Eq. (7), see below for details] based upon the temperature and supersaturation profiles in the nucleation chamber is plotted for 1-propanol (see below for a description of this calculation). The rate of nucleation is zero throughout most of the nucleation chamber. However, just before the maximum in the supersaturation in the center portion of the chamber (i.e., closer to the entrance of the chamber), the calculated value of the nucleation rate exceeds zero, rises to a maximum, and then decays to zero further down the chamber. For the helium experiments, this prediction corresponds well to the region in the nucleation chamber where we observe nucleation to occur in these experiments. Also, the predicted rate shown in the figure agrees well with the observed rate of nucleation (1–5 drops/cm^3/s). For the argon experiments, the region where the onset of nucleation is predicted to occur (see Fig. 13) corresponds approximately (but less well) to the region where nucleation is observed to occur, and the observed rate is orders of magnitude larger than

TABLE V. Thermodynamic and hydrodynamic data for 1-propanol, helium, argon, nitrogen, and hydrogen. Expressions are given for saturation vapor pressure, P_{01}, thermal conductivity, λ, vapor viscosity, η_v, molar heat capacity for vapor, C_p, molecular weight, M_w, liquid density, ρ_l, surface tension, σ, binary diffusion coefficient, D_{12}, and the binary diffusion coefficient temperature dependence, s.[a]

1-Propanol

$P_{01}=10^{(9.45-2432/T)}$[b]

$\lambda=6.19813\times10^{-5}[\exp(8.64542\times10^{-5}T)-\exp(-4.494\,13\times10^{-4}T)]+2.460\,71\times10^{-10}T^{2}$[c]

$\eta_v=1.183\times10^{-5}\left[\frac{T^{1.5}}{T+506.75}\right]^{d}$

$C_p=0.59+0.079\,42T-4.431\times10^{-5}T^{2}+1.026\times10^{-8}T^{3}$[e]

$M_w=60.096$

$\rho_l=0.8201-0.000\,818\,3(T-273.16)+1.06\times10^{-6}(T-273.16)^{2}+1.65\times10^{-8}(T-273.16)^{3}$[f]

$\sigma=24.95-0.0772(T-273.16)$[g]

D_{12} (He, 273.16, 1.013 bar)$=0.306\,27$[h]; $s=0.75$[i]

D_{12} (Ar, 273.16, 1.013 bar)$=0.084\,31$[h]; $s=0.75$[i]

D_{12} (N_2, 273.16, 1.013 bar)$=0.092\,01$[h]; $s=0.75$[i]

D_{12} (H_2, 273.16, 1.013 bar)$=0.355\,92$[h]; $s=0.75$[i]

Helium

$\lambda=7.376\,974\times10^{-5}+1.139\,222\times10^{-6}T-6.343\,536\times10^{-10}T^{2}$[j]

$\eta_v=145.5\times10^{-7}\left[\frac{T^{1.5}}{T+74.1}\right]^{d}$

$C_p=4.968$[e]

$M_w=4.0026$

Argon

$\lambda=-1.3\times10^{-6}+1.76\times10^{-7}T-1.1\times10^{-10}T^{2}+3.44\times10^{-14}T^{3}$[k]

$\eta_v=1.956\,55\times10^{-5}\left[\frac{T^{1.5}}{T+141.59}\right]^{d}$

$C_p=4.968$[e]

$M_w=39.948$

Nitrogen

$\lambda=(9.3718\times10^{-7}+2.348\times10^{-7}T-1.212\times10^{-10}T^{2}+3.597\times10^{-14}T^{3})$[l]

$\eta_v=12.6144\times10^{-6}\left[\frac{T^{1.5}}{T+64.67}\right]^{d}$

$C_p=7.452-3.246\times10^{-3}T+6.4114\times10^{-6}T^{2}-2.794\times10^{-9}T^{3}$[e]

$M_w=28.013$

Hydrogen

$\lambda=(19.3728\times10^{-6}+1.6\times10^{-6}T-9.945\times10^{-10}T^{2}+3.736\times10^{-13}T^{3})$[l]

$\eta_v=6.246\times10^{-6}\left[\frac{T^{1.5}}{T+55.34}\right]^{d}$

$C_p=6.952-0.045\,76\times10^{-2}T-0.095\,63\times10^{-5}T^{2}-0.2079\times10^{-9}T^{3}$[m]

$M_w=2.016$

[a]Units: P_{01} in mm Hg; λ in Cal/(cm s K); η_v in Poise; C_p in cal/(mol K); ρ_l in g/cm^3; σ in dyn/cm; D_{12} in cm^2/s, and s is dimensionless.
[b]See Ref. 29.
[c]See Ref. 30.
[d]See Ref. 31.
[e]See Reference 20, Appendix A, pp. 656–732.
[f]See Ref. 32.
[g]See Ref. 33.
[h]See Ref. 34.
[i]See Ref. 20, pp. 595–596.
[j]See Ref. 35.
[k]See Ref. 36.
[l]See Ref. 20, pp. 515–517.
[m]See Ref. 37.

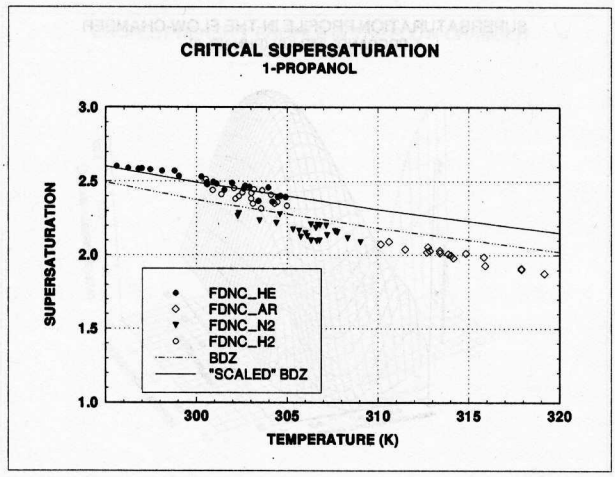

FIG. 6. Variation of the critical supersaturation of 1-propanol with temperature obtained in this investigation using as background gas helium (solid circle), hydrogen (open circle), nitrogen (solid triangle), and argon (open diamond). Also shown for purposes of comparison only are the predictions of the BDZ nucleation theory (dash dot dot dot line) and a "scaled" version of the BDZ theory (solid line) described in Ref. 2 (see the text for discussion).

predicted in Fig. 13. We shall return to this point later in this section. As is seen in Figs. 9 and 13, the nucleation observed in the argon background gas experiments occurred further down the nucleation chamber than in the helium experiments.

While the nucleation rate profiles shown in Figs. 9 and 13 are useful in determining where nucleation occurs, what is actually observed is the integrated number of droplets nucleated and grown to observable size. This profile of nucleated droplet density is shown for these two examples in Figs. 10 and 14. In both of these figures, the onset of nucleation is shown followed by an increase in the number of nucleated droplets which eventually reaches a constant num-

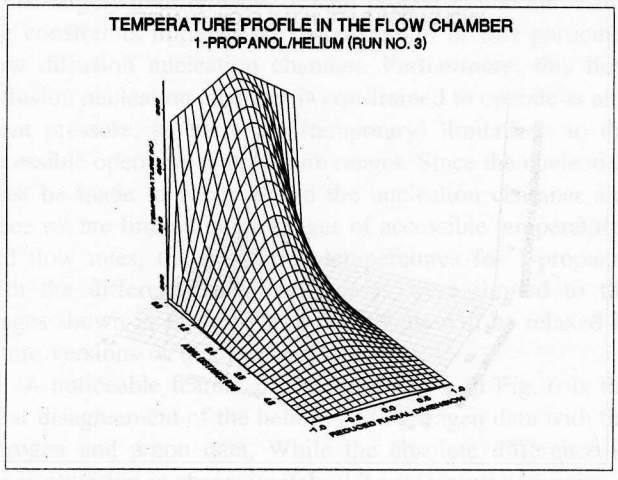

FIG. 7. Computed three-dimensional perspective surface showing the temperature profile in the nucleation chamber for run 3 of the 1-propanol/helium investigation.

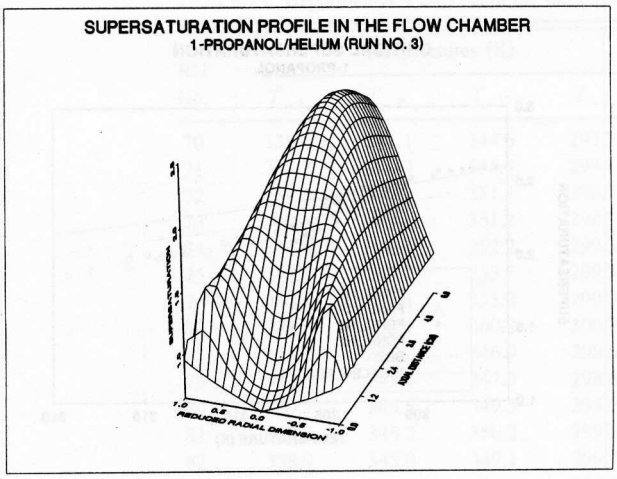

FIG. 8. Computed three-dimensional perspective surface showing the supersaturation profile in the nucleation chamber for run 3 of the 1-propanol/helium investigation.

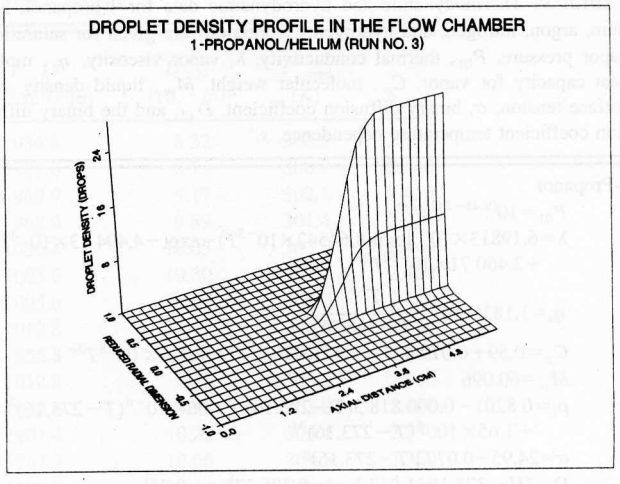

FIG. 10. Computed three-dimensional perspective surface showing the nucleated droplet density profile in the nucleation chamber for run 3 of the 1-propanol/helium investigation.

ber of droplets flowing down the chamber. Again, the droplet density profile for the argon experiments is shown occurring farther down the chamber than that obtained during the helium experiments, and the number of argon droplets predicted using Eq. (7) is orders of magnitude smaller than actually observed in our experiments (see below for more details).

The comparison, shown in Fig. 5, of the 1-propanol/helium system critical supersaturation versus temperature data obtained using the flow diffusion cloud chamber and that obtained using a thermal diffusion cloud chamber (the envelope of the dashed line curves) illustrates the quantitative agreement of these two sets of data. This agreement not only confirms the utility of this flow diffusion cloud chamber, but it also provides additional support for the thermal diffusion cloud chamber data. The predicted variation of the critical supersaturation of 1-propanol with temperature according to the BDZ theory is shown in Fig. 5 for comparison purposes only. The "scaled" predicted variation of the critical supersaturation also shown in Fig. 5 was obtained using

$$J = J_{\mathrm{BDZ}} \exp - \left(a - \frac{b}{T} \right), \tag{7}$$

where J is the observed nucleation rate (1–5 drops/cm^3/s in our experiments), J_{BDZ} is the BDZ expression for the rate of homogeneous nucleation, T is the absolute temperature, and a and b are constants. Equation (7) and the values of a and b used in this calculation ($a=61.65$ and $b=16670.4$) were taken from Ref. 2. Since the values of a and b were chosen (in Ref. 2) to provide a good fit to the thermal diffusion cloud chamber data for the 1-propanol/helium system, the good agreement of Eq. (7) with the flow diffusion cloud

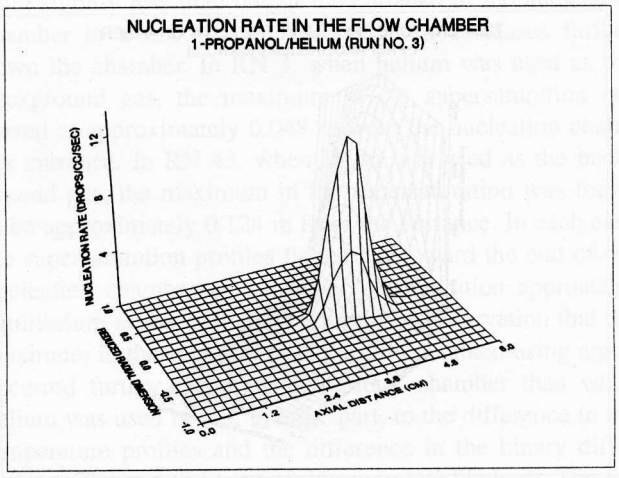

FIG. 9. Computed three-dimensional perspective surface showing the nucleation rate profile in the nucleation chamber for run 3 of the 1-propanol/helium investigation.

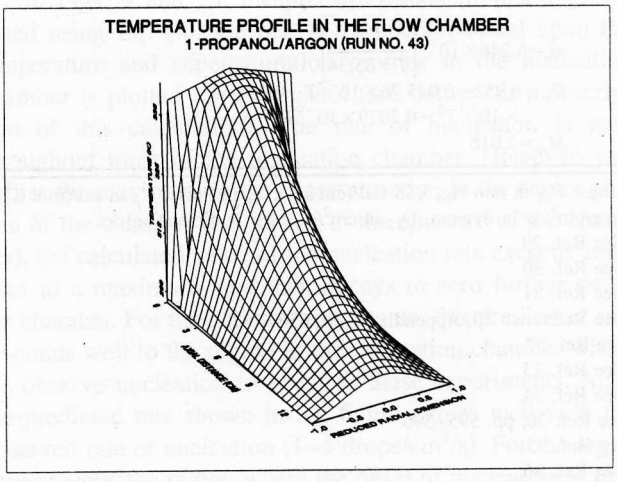

FIG. 11. Computed three-dimensional perspective surface showing the temperature profile in the nucleation chamber for run 43 of the 1-propanol/argon investigation.

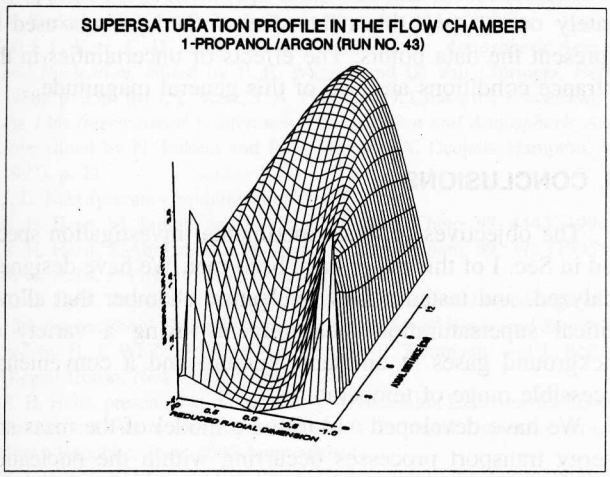

FIG. 12. Computed three-dimensional perspective surface showing the supersaturation profile in the nucleation chamber for run 43 of the 1-propanol/argon investigation.

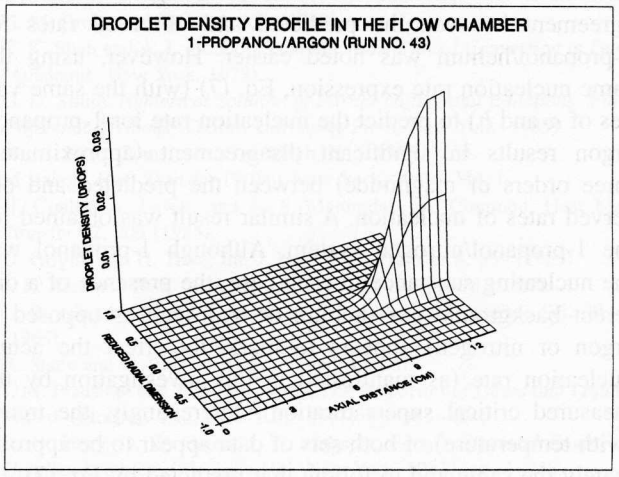

FIG. 14. Computed three-dimensional perspective surface showing the nucleated droplet density profile in the nucleation chamber for run number 43 of the 1-propanol/argon investigation.

chamber data is consistent with the good agreement of the thermal diffusion cloud chamber data plotted in Fig. 5. We note that the purpose of defining the scaling exponential factor containing the a and b terms in Eq. (7) was to obtain an expression useful for accurately reproducing nucleation rate data for scientific and engineering applications.[2] In this instance, it has proven to be particularly useful in comparing the variation of the critical supersaturation with temperature for 1-propanol obtained with the thermal diffusion cloud chamber and that obtained with the flow diffusion cloud chamber (particularly when using different background gases, see below).

In Fig. 6, we compare the 1-propanol critical supersaturation versus nucleation temperature data obtained using the flow diffusion cloud chamber when helium, hydrogen, argon, and nitrogen were used as background gases. Again, the predicted variation of the critical supersaturation of 1-propanol with temperature according to the BDZ theory is shown for comparison purposes only, and the scaled predicted variation of the critical supersaturation also shown was obtained using Eq. (7). We note from the data plotted in Fig. 6 the rather close agreement between the helium and hydrogen data. The agreement between the helium data and Eq. (7) has already been noted. The agreement between the helium and hydrogen data is consistent with other diffusion cloud chamber data obtained for alcohol vapors under near ambient (and below) pressures and temperatures in this range (and lower) reported in the literature.[2,27]

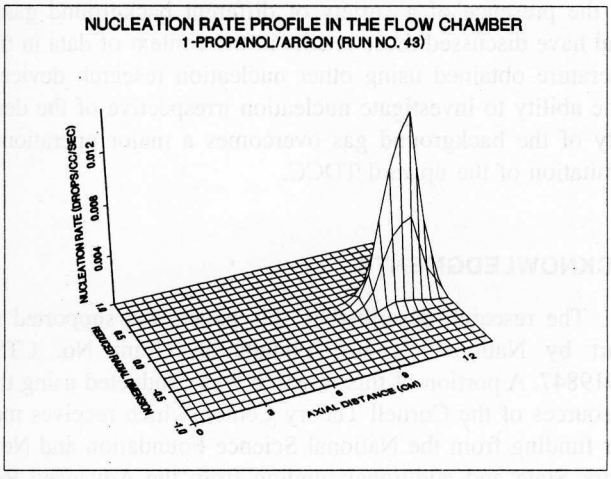

FIG. 13. Computed three-dimensional perspective surface showing the nucleation rate profile in the nucleation chamber for run 43 of the 1-propanol/argon investigation.

In Fig. 6, we note the agreement between the 1-propanol critical supersaturation data obtained when argon and when nitrogen were used as background gases. The reason (1) the nitrogen and argon data do not overlap, (2) the overlap of the nitrogen, helium, and hydrogen data is limited, and (3) the overlap of the helium and hydrogen data is somewhat limited is due largely to differences in their properties and the resulting constraints imposed on the operation of this particular flow diffusion nucleation chamber. Furthermore, this flow diffusion nucleation chamber is constrained to operate at ambient pressure, so there are (temporary) limitations to the accessible operating temperature ranges. Since the nucleation must be made to occur within the nucleation chamber and since we are limited in the ranges of accessible temperatures and flow rates, the nucleation temperatures for 1-propanol with the different background gases were limited to the ranges shown in Fig. 6. These constraints will be relaxed in future versions of this flow chamber.

A noticeable feature of the data shown in Fig. 6 is the clear disagreement of the helium and hydrogen data with the nitrogen and argon data. While the absolute difference in supersaturation is approximately 0.2 supersaturation units, it is observable and reproducible. This difference is also manifested in the nucleation rate calculations shown in Figs. 9 and 13. As described above, Eq. (7) was used to predict the

nucleation rate profiles shown in these figures. The good agreement between the predicted and observed rates for 1-propanol/helium was noted earlier. However, using the same nucleation rate expression, Eq. (7) (with the same values of a and b) to predict the nucleation rate for 1-propanol/argon results in significant disagreement (approximately three orders of magnitude) between the predicted and observed rates of nucleation. A similar result was obtained for the 1-propanol/nitrogen system. Although 1-propanol was the nucleating substance in each case, the presence of a different background gas (helium or hydrogen as opposed to argon or nitrogen) appears to markedly effect the actual nucleation rate (as manifested in this investigation by the measured critical supersaturation). Interestingly, the trends (with temperature) of both sets of data appear to be approximately the same and to follow that predicted by Eq. (7).

The dependence of nucleation rate upon the kind (and amount) of background gas has been observed before. In Refs. 5 and 6, the authors reported significant differences in the nucleation of methanol, ethanol, 1-propanol, and 2-propanol at elevated pressures and temperatures (as manifested through the measurement of the critical supersaturation) when either helium or hydrogen was used as a background gas. It should be noted, however, that these differences became less distinct as the total pressure approached ambient which is consistent with the results obtained in this investigation. Behavior similar to that observed for the four alcohols has been reported for the nucleation of 1-butanol in the presence of helium, hydrogen, and nitrogen.[9] Furthermore, it has been reported that the nucleation rate of water measured in an expansion cloud chamber was greater using argon as the background gas than when helium was used as the background gas.[28] It needs to be pointed out, however, that there have also been a number of investigations described in the literature in which the background gas did not appear to effect the nucleation of a particular vapor. A number of these investigations are described in Refs. 5 and 8. In any case, what is clear is that the role of the background gas in the nucleation process is still uncertain and remains a controversial issue and needs to be resolved. If there is an effect of background gas on nucleation, all current models of nucleation will need to be revised to reflect this dependence. Furthermore, since nucleation is playing an increasingly greater technological role in areas such as ultrafine particle production, it is essential that the role of any other substances present during the nucleation process be well understood.

The critical supersaturation data shown in Figs. 5 and 6 were obtained repeatedly and reproducibly over a period of nearly one year. What small variation exists in the data arises primarily from the uncertainty in observing the exact position of the onset of nucleation. A variation of ± 0.001 m in the location of the region where nucleation begins corresponds to a difference of the order of ± 0.02 in the critical supersaturation. A sensitivity analysis of the data taking into account uncertainties in the thermodynamic and hydrodynamic data (shown in Table V) used in our analysis of the temperature and supersaturation conditions in the nucleation chamber indicate variations in the plotted data to be approximately one to two times the size of the symbols used to represent the data points. The effects of uncertainties in the entrance conditions are also of this general magnitude.

VI. CONCLUSIONS

The objectives of this experimental investigation specified in Sec. I of this paper have been met. We have designed, analyzed, and tested a flow nucleation chamber that allows critical supersaturation measurements using a variety of background gases at ambient pressure and a conveniently accessible range of temperatures.

We have developed and tested a model of the mass and energy transport processes occurring within the nucleation chamber. Although the model works well for the conditions used during these experiments, our analysis suggests that some improvement can be realized by incorporating second-order axial dispersion effects into the analysis. This will be done in a subsequent refinement of the model description. The limited ranges of pressure and temperature accessible to this particular device result only from our desire to first carefully study and quantify the operation of this device in order that extending these operating ranges can be accomplished in an orderly and well-defined manner.

We have tested the quantitative operation of this nucleation chamber by comparing data obtained from our nucleation measurements with data available in the literature obtained using a thermal diffusion cloud chamber and thereby demonstrated that this device is capable of quantitative investigations of vapor nucleation. While critical supersaturation measurements were the objective of this investigation, nucleation rate measurements are also desirable. This nucleation chamber was designed to allow convenient optical access to the nucleation zone which will facilitate quantitative nucleation rate measurements. Consistent with our stated goals, the capability of nucleation rate measurement will be included as part of the next version of this chamber.

We have made preliminary measurements of nucleation in the presence of a variety of different background gases and have discussed those results in the context of data in the literature obtained using other nucleation research devices. The ability to investigate nucleation irrespective of the density of the background gas overcomes a major operational limitation of the upward TDCC.

ACKNOWLEDGMENTS

The research described in this paper was supported in part by National Science Foundation Grant No. CTS-8919847. A portion of this research was conducted using the resources of the Cornell Theory Center, which receives major funding from the National Science Foundation and New York State and additional funding from the Advanced Research Projects Agency, the National Institute of Health, IBM Corporation, and other members of the Theory Center's Corporate Research Institute.

[1] R. H. Heist and H. He, J. Phys. Chem. Ref. Data **23**, 781 (1994).
[2] A. Kacker and R. H. Heist, J. Chem. Phys. **82**, 2734 (1985).
[3] (a) J. L. Katz, C.-H. Hung, and M. J. Krasnopoler, *Atmospheric Aerosols and Nucleation*, edited by P. E. Wagner and G. Vali (Springer, Berlin, 1988), p. 356; (b) J. L. Katz, J. A. Fisk, and V. Chakarov, *Proceedings of the 13th International Conference on Nucleation and Atmospheric Aerosols*, edited by N. Fukuta and P. E. Wagner (A. Deepak, Hampton, VA, 1992), p. 11.
[4] J. L. Katz (private communication).
[5] R. H. Heist, M. Janjua, and J. Ahmed, J. Phys. Chem. **98**, 4443 (1994).
[6] R. H. Heist, J. Ahmed, and M. Janjua, J. Phys. Chem. **99**, 375 (1995).
[7] R. H. Heist, J. Phys. Chem. (in press).
[8] R. H. Heist, *Physical Chemistry of Aqueous Systems, Proceedings of the 12th International Conference on the Properties of Water and Steam*, edited by H. J. White, Jr., J. V. Sengers, D. B. Neumann, and J. Bellows (Begell House, New York, 1995), p. 286.
[9] R. H. Heist, presented at the workshop—Nucleation Experiments: State of the Art and Future Developments, Czech Technical University, Prague, Czech Republic, June, 1995 (unpublished).
[10] Y. Viisanen, R. Strey, and H. Reiss, J. Chem. Phys. **99**, 4680 (1993).
[11] J. Schmidt (private communication).
[12] R. Strey (private communication).
[13] V. Vohra, Ph.D. thesis, University of Rochester, 1995.
[14] H. L. Langhaar, J. Appl. Mech. **9**, 55 (1942).
[15] P. J. Schneider, Trans. ASME **79**, 765 (1957).
[16] V. G. Kostrovskii, V. B. Mikheev, and M. S. Shtein, Kolloidn. Zh. **44**, 773 (1982).
[17] R. C. Reid, J. M. Prausnitz, and B. E. Poling, *The Properties of Gases and Liquids*, 4th ed. (McGraw-Hill, New York, 1987).
[18] L. Graetz, Ann. Phys. **18**, 79 (1883).
[19] W. Nusselt, Z. Ver. deut. Ing. **54**, 1154 (1910).
[20] G. M. Brown, AIChE J. **6**, 179 (1960).
[21] R. K. Shah and A. L. London, *Laminar Flow Forced Convection in Ducts* (Academic, New York, 1978).
[22] G. D. Smith, *Numerical Solution of Partial Differential Equations: Finite Difference Methods* (Oxford University Press, New York, 1985).
[23] W. M. Kays, Trans. Am. Soc. Mech. Eng. **1955**, 1256.
[24] M. Jakob, *Heat Transfer* (Wiley, New York, 1949), Vol. I.
[25] N. Conley, A. Lawal, and A. S. Majumdar, Int. Commun. Heat Mass Transfer **12**, 209 (1985).
[26] U. Grigull and H. Tratz, Int. J. Heat Mass Transfer **8**, 669 (1965).
[27] J. L. Katz and B. J. Ostermier, J. Chem. Phys. **47**, 478 (1967).
[28] L. B. Allen and J. L. Kassner, Jr., J. Colloid and Interface Sci. **30**, 81 (1969).
[29] R. Stacy and C. Reid (private communication).
[30] J. M. Prausnitz and T. K. Sherwood, *The Properties of Gases and Liquids*, 3rd ed. (McGraw Hill, New York, 1977), pp. 481–494.
[31] R. H. Perry, D. W. Green, J. O. Maloney, *Perry's Chemical Engineer's Handbook*, 6th ed. (McGraw-Hill, New York, 1983), pp. 3–248.
[32] *International Critical Tables* (McGraw-Hill, New York, 1929), Vol. 3, pp. 27–29.
[33] J. L. Katz and B. J. Ostermier, J. Chem. Phys. **47**, 478 (1987).
[34] E. N. Fuller, P. S. Schettler, and J. C. Riddings, Ind. Eng. Chem. **58**, 19 (1911).
[35] R. H. Heist and H. Reiss, J. Chem. Phys. **59**, 15 (1973).
[36] Y. S. Touloukian, P. E. Liley, and S. C. Sayena, *Thermophysical Properties of Matter* (IRI/Plenum, New York, 1970), Vol. 3.
[37] S. I. Sandler, *Chemical and Engineering Thermodynamics*, 2nd. ed. (Wiley, New York, 1989), pp. 583.